ACS APPLIED MATERIALS & INTERFACES

Research Article

Cite This: ACS Appl. Mater. Interfaces 2019, 11, 42288−42297

www.acsami.org

Unveiling Carbon Ring Structure Formation Mechanisms in Polyacrylonitrile-Derived Carbon Fibers

Jiadeng Zhu,[†] Zan Gao,[†] Malgorzata Kowalik,[‡] Kaushik Joshi,[§] Chowdhury M. Ashraf,[‡] Mikhail I. Arefev,[§] Yosyp Schwab,[†] Clifton Bumgardner,[†] Kenneth Brown,[†] Diana Elizabeth Burden,[†] Liwen Zhang,[†] James W. Klett,[∥] Leonid V. Zhigilei,*[,§] Adri C. T. van Duin,*[,‡] and Xiaodong Li*[,†]

[†]Department of Mechanical and Aerospace Engineering, University of Virginia, 122 Engineer's Way, Charlottesville, Virginia 22904, United States

[‡]Department of Mechanical Engineering, Pennsylvania State University, University Park, Pennsylvania 16802, United States

[§]Department of Materials Science and Engineering, University of Virginia, 395 McCormick Road, Charlottesville, Virginia 22904, United States

[∥]Oak Ridge National Laboratory, Oak Ridge, Tennessee 37831, United States

Supporting Information

ABSTRACT: As the demand for electric vehicles (EVs) and autonomous vehicles (AVs) rapidly grows, lower-cost, lighter, and stronger carbon fibers (CFs) are urgently needed to respond to consumers' call for greater EV traveling range and stronger safety structures for AVs. Converting polymeric precursors to CFs requires a complex set of thermochemical processes; a systematic understanding of each parameter in fiber conversion is still, to a large extent, lacking. Here, we demonstrate the effect of carbonization temperature on carbon ring structure formation by combining atomistic/microscale simulations and experimental validation. Experimental testing, as predicted by simulations, exhibited that the strength and ductility of PAN CFs decreased, whereas the Young's modulus increased with increasing carbonization temperature. Our simulations unveiled that high carbonization temperature accelerated the kinetics of graphitic phase nucleation and growth, leading to the decrease in strength and ductility but increase in modulus. The methodology presented herein using combined atomistic/microscale simulations and experimental validation lays a firm foundation for further innovation in CF manufacturing and low-cost alternative precursor development.

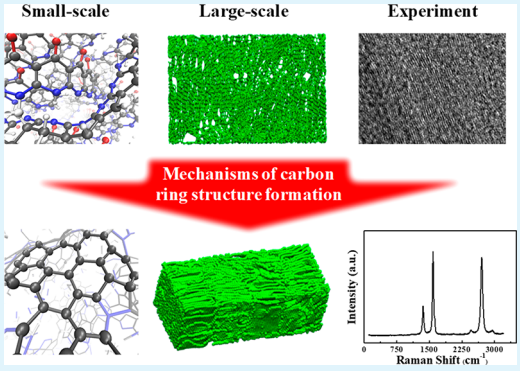

KEYWORDS: *carbon fibers, carbon ring structure formation mechanisms, atomistic simulation, microscale simulation, experimental validation*

1. INTRODUCTION

Since their initial development in the 1940s, carbon fibers (CFs) have been a critical engineering material for high-performance and extreme environment applications because of their unique mechanical properties (high strength/modulus), competitive dimensional stability, low coefficient of thermal expansion, and excellent thermal and electrical conductivities.[1−10] The demand for CFs is growing rapidly as the vehicle manufacturing and power generation industries require lighter and stronger materials to meet their customers' efficiency and safety expectations.[11−20] Typically, CFs are produced by thermochemically converting one of three classes of precursor fibers into CFs: polyacrylonitrile (PAN), rayon, or pitch.[21−28] Among the three types, PAN is most commonly used (>90% of CF production globally) because its conversion results in a relatively high carbon yield, which gives rise to a thermally stable and well-oriented carbon fiber microstructure.[29−35]

The mechanical properties of PAN-based CFs are highly dependent on the myriad process parameters involved in the stabilization and carbonization processes required to convert the precursor fibers to CFs.[36−40] Great effort has been dedicated to fine-tuning the process parameters via numerical simulations and experimental testing.[41−49] For example, Gupta et al.[47] studied the structural changes in the precursor fibers during the oxidative stabilization and found that reactions initiated in amorphous parts of the copolymer of acrylonitrile, methyl acrylate, and itaconic acid at temperatures below 500 K contribute significantly to the macroscopic shrinkage of the fibers. The research carried out by Lee and his group[48] demonstrated that the stabilization process could be assisted by a radio frequency capacitive plasma discharge, enhancing

Received: September 2, 2019
Accepted: October 28, 2019
Published: October 28, 2019

DOI: 10.1021/acsami.9b15833
ACS Appl. Mater. Interfaces 2019, 11, 42288−42297

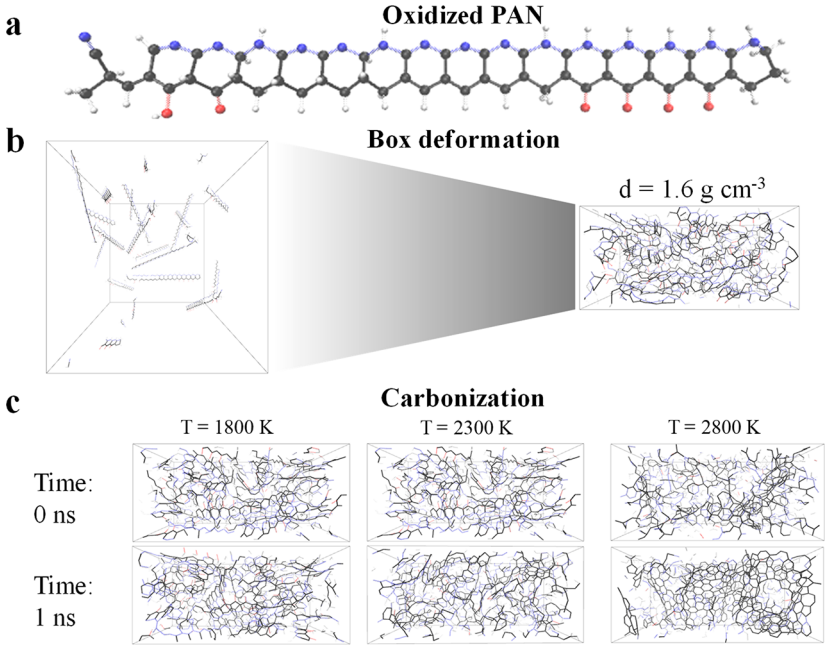

Figure 1. An overview of the ReaxFF simulations. (a) The atomic representation of the oxidized PAN molecule. The bonds between carbon atoms are solid black lines, and the bonds involving nitrogen, oxygen, and hydrogen atoms are represented by blue, red, and white lines, respectively. The atoms are represented as solid spheres: black, carbon; blue, nitrogen; red, oxygen; and white, hydrogen atoms. (b) A construction of the simulations box showing the gradual deformation of an initial 16 oxidized PAN molecules, placed randomly in the cubic box with a size of 80 Å, such that the final density of the system is 1.6 g cm^{-3}. (c) Snapshots of one representative sample for each of the considered carbonization temperatures, 1800, 2300, and 2800 K, at the beginning (time of 0 ns) and at the end of the carbonization simulations (time of 1 ns).

the final mechanical properties of CFs. Saha et al.[46] studied the carbonization mechanism of idealized ladder PAN in atomistic simulations performed with the ReaxFF potential and observed a correlation between carbon ring production and carbonization temperature. Recently, Kim et al.[39] experimentally found that a slow heating rate during the carbonization process could improve the strength of the resultant CFs. The increase in strength was attributed to the increase of both the fraction of carbon with sp^3 bonding and the number of nitrogen atoms with quaternary bonding in the hexagonal carbon network. These prior studies provide a strong indication that stabilization and carbonization processes have dominant effects on the atomic-scale structure and mechanical properties of CFs. However, a complete understanding of the correlation between the carbonization process, fiber microstructure, and mechanical properties of CFs is still lacking and can only be obtained through a comprehensive, multiscale investigation that combines computational and experimental efforts.

In this study, we focused on elucidating the influence of the carbonization temperature on the carbon ring structure development in PAN-based CFs using detailed experimental characterization and multiscale modeling (from atomistic-scale to microscale) to unveil the carbon ring formation mechanism. The results of this study will not only equip the research community with a broad view of the PAN-based CF conversion process but also provide a simulation framework to select and evaluate alternative precursor materials that may result in cheaper and stronger CFs.

2. EXPERIMENTAL AND SIMULATION METHODS

2.1. Synthesis of PAN-Based CFs. Oxidized PAN fibers with a density of 1.401 g cm^{-3} were obtained from Bluestar Fibers, Co. Ltd., and were carbonized at three separate temperatures, 1800, 2300, or 2800 K, for 30 min with a heating rate of 10 K min^{-1} in a nitrogen atmosphere with a flowing rate of 38 scfh at Oak Ridge National Laboratory. The carbonized fibers were characterized after naturally cooling to room temperature in the furnace and yielded densities of 1.746, 1.772, and 1.858 g cm^{-3}, respectively.

2.2. Characterization of Prepared CFs. The morphology of CFs was investigated using field-emission scanning electron microscopy (FE-SEM, FEI Quanta 650) and high-resolution transmission electron microscopy (HR-TEM, FEI Titan). To prepare samples for HR-TEM, CFs were dispersed in ethanol and deposited on a Cu grid. Elemental analysis of the processed CFs was performed using a PerkinElmer 2400 Series II CHNS/O. X-ray diffraction (XRD, PANalytical X'Pert Pro Multi-Purpose diffractometer) patterns were recorded on a Rigaku D/max 2400, Japan, with Cu Kα (λ = 1.5406 Å) radiation in the 2θ range from 10° to 80°. Raman spectroscopy (Renishaw InVia equipped with a 514 nm laser beam) was performed to detect the graphitic carbon structure and the presence of defects in the processed CFs. X-ray photoelectron spectroscopy (XPS, PHI VersaProbe III) was used to verify the aforementioned elemental analysis and identify surface functional groups of the CFs at room temperature using a Kratos Analytical spectrometer and monochromatic Mg Kα X-ray source. The densities of oxidized PAN and carbonized fibers were measured using a gas pycnometer (Micromeritics AccuPyc II 1340, U.S.). The ASTM D3822 standard was used to guide the uniaxial tensile tests of individual single fibers (30 or more filament-tests for each CF) using a MTS/Keysight UTM T150 tester with a cross head speed of 10^{-4} mm min^{-1} and 20 mm specimen gauge length. Young's modulus, E, was determined by the ratio of the strength along an axis over the strain along that axis in the initial part of the stress−strain dependence. The mean values of the strength, strain, and Young's modulus of each CF have been provided on the basis of the number of tested samples for each CF in this work. The corresponding error value is the standard deviation from the mean.

2.3. Computational Models. To gain an atomistic/microscopic understanding of the effect of carbonization temperature on structure and properties of CFs, a series of multiscale simulations were carried out. The chemical and structural transformations during carbonization

DOI: 10.1021/acsami.9b15833
ACS Appl. Mater. Interfaces 2019, 11, 42288−42297

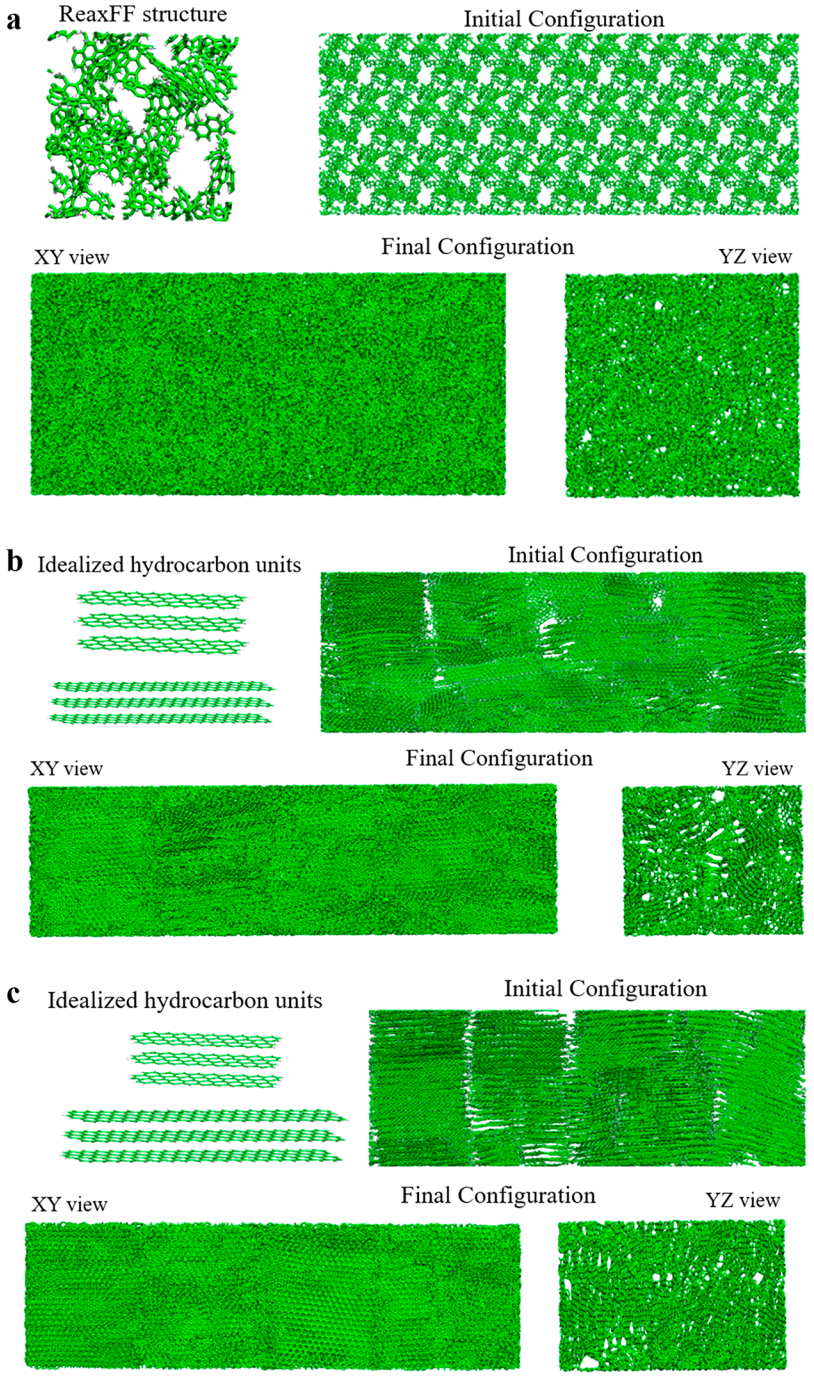

Figure 2. Structural units, and initial and final configurations of three microstructures of CF fibers generated in large-scale atomistic simulations. The microstructure shown in (a) consists of 116 600 carbon atoms and is referred to as MS1. The microstructures shown in (b) and (c) consist of 115 200 atoms each and are referred to as MS2 and MS3, respectively. Carbon and hydrogen atoms are colored green and white, respectively. Only 4 nm-thick slices of the systems are shown in the transverse (*YZ*) views.

occur over a time scale of minutes or hours, which is not accessible to atomistic simulations. Thus, in the atomistic simulations reported in this Article, we do not attempt to simulate the carbonization process at experimental time scales but focus on two critical aspects related to the dependence of the microstructure and properties of CFs on carbonization temperature. In the first series of simulations, we investigate the possible channels of the graphitic structure formation from the precursor polymer at the initial stage of the carbonization process. The simulations of reactive carbonization from oxidized PAN precursor molecules were performed with the ReaxFF reactive force field recently adapted for C/H/O/N-based polymer carbonization simulations, and the evolution of all-carbon rings at various carbonization temperatures was investigated. In the second series of simulations, we explore the effect of the degree of graphitization and structural alignment within the CF microstructure on the mechanical properties of CFs. To achieve a realistic representation of CF microstructure, the length-scale of the simulations must be significantly increased, which was made possible using a more computationally efficient AIREBO-M potential. More details on the computational setups used in each set of the simulations are provided in the following two subsections.

2.3.1. Atomic-Scale ReaxFF Simulations. ReaxFF interatomic potentials are the bond-order[50,51] interatomic potentials that are trained on the basis of available empirical or quantum mechanical

DOI: 10.1021/acsami.9b15833
ACS Appl. Mater. Interfaces 2019, 11, 42288−42297

data. Unlike classical force fields, ReaxFF can simulate chemical bond formation and bond breaking on-the-fly, which enables us to simulate chemically reactive complex systems using molecular dynamics (MD) method. An overview of the ReaxFF method can be found in a recent review paper.[52] While the data presented by Saha et al.[34] were encouraging, the available ReaxFF was not suitable for simulation of the PAN molecule where oxygen atoms are included. For the simulation reported in this Article, we used the recently published ReaxFF parameter set[53] that allows us to consider more realistic stabilized PAN molecules,[54] including oxygen atoms in the polymer structure. This recently published ReaxFF parameter set has the carbon parameters, which are suitable for the reasonable estimation of the graphene properties,[55] and it accounts for the C/H/O chemistry for small molecules[56] and stable nitrogen production as well. This newly developed ReaxFF parameter set is an extension of Ashraf et al.'s[56] C/H/O-2016 ReaxFF implementation with the use of ADF simulation software.[57]

A stabilized PAN molecule based on experimental data[54] was utilized as an elementary unit for building an atomistic model of the oxidized PAN chain considered in our simulations (see Figure 1a). Initially, 16 of these chains were placed randomly in the simulation box by applying periodic boundary conditions, and then the system was gradually deformed, as schematically presented in Figure 1b, such that the final density of the system was comparable to the experimental density, 1.6 g cm^{-3}, of oxidized PAN samples.[58] This box of the oxidized PAN polymers was then equilibrated at a temperature of 300 K for 100 ps using an *NVT* ensemble, where number of atoms, *N*, volume of the simulation box, *V*, and temperature, *T*, were kept constant. Three different configurations from the final 30 ps of this equilibration simulation were taken as the starting configurations for three independent simulations. In each of these three simulations, the samples were heated at 10 K ps^{-1} from 300 to 1800, 2300, and 2800 K. The carbonization simulations were then performed by keeping the systems at each of the considered carbonization temperatures for 1 ns. The snapshots of the simulation box at the beginning and after 1 ns of the carbonization simulations for each of the considered temperatures are presented in Figure 1c. All presented snapshots in this study were generated with use of visual molecular dynamics (VMD).[59]

2.3.2. Large-Scale Simulations for CF Microstructures. The experimental results discussed in the next section show that the graphite content of the microstructure of CF increases with the carbonization temperature. To capture this temperature effect on microstructure and to reveal the implications on the mechanical properties, we generated three large-scale atomistic models of CF microstructures with different levels of graphitization. The microstructures were produced using a computationally efficient method based on structural self-organization and reactive fusing of carbon ladder structural units. A detailed description of the method is provided in our previous study.[60]

The first microstructure (MS1) was prepared by using carbon clusters obtained in a smaller-scale ReaxFF MD simulation following a procedure similar to that described in section 2.3.1. The ReaxFF simulation was performed for idealized PAN molecules (nonoxidized) at 2800 K. During the ReaxFF simulation, some molecules reacted with each other, forming clusters/sheets of five- to nine-member rings. After the partially reacted system was quenched to room temperature, H and N atoms were deleted from the ReaxFF simulation cell, and then only the carbon atoms that were part of five- to nine-member carbon rings were selected. Hydrogen atoms were then added to saturate carbon atoms. The resulting structure, which is periodic in all three directions, was used as a basic structural unit for creating microstructure MS1 (Figure 2a). The initial configuration of the first microstructure was obtained by replicating the structural unit 8 times in *x*-direction and 3 times in *y*- and *z*-directions each.

For the other two microstructures, MS2 and MS3, we used two idealized hydrocarbon units shown in Figure 2b and c. Each of these two units is a block of three carbon ladders stacked into Bernal arrangement, with each ladder consisting of three rows of six-member carbon rings. The length of the two structural units is 2.3 and 4.8 nm. The initial configurations were generated using PACKMOL.[61] In the generation of microstructure MS2, the two units were aligned preferentially along the fiber axis (±10° with respect to *x*-axis) with no orientation constraints applied in the transverse directions. The initial configuration of microstructure MS3 was obtained by aligning the two units in both longitudinal and transverse directions (within ±4° with respect to the three axis). In both MS2 and MS3 microstructures, each of the two units represents 50% of the structure by weight.

The generation of the initial configurations was followed by a sequence of MD simulations aimed at obtaining the final CF microstructures. The sequence of MD simulations includes energy minimization of initial configurations, room temperature equilibration of the energy minimized structures, and removal of hydrogen atoms followed by thermal annealing. A detailed description of the procedure used in the preparation of CF computational samples is provided in our previous study.[60] The MD simulations were performed using reactive AIREBO-M potential[62] implemented within LAMMPS suite.[63] The AIREBO potential provides a reasonably accurate description of reactive dynamics in hydrocarbon systems at a moderate computational cost, thus enabling large-scale MD simulations for systems consisting of more than 10^5 atoms.

The simulated microstructures were characterized to identify structural characteristics, such as XRD profiles and d_{002} spacing, crystallite size, degree of graphitization, and ring alignment. Detailed discussion of the methods used for structural characterization of the computational samples is provided in our previous study.[60] XRD profiles were obtained by integrating the radial distribution function of each microstructure. The position of (002) peak of an XRD profile was then used to identify the interlayer *d*-spacing. The size of graphitic crystallites was estimated using Scherrer's equation. To evaluate the degree of graphitization, we used per atom energy and hybridization state of carbon atoms. Any carbon atom that has sp^2 hybridization state and energy within 30 meV from the energy of a carbon atom in an ideal graphite crystal was tagged as an atom that belongs to a graphitic region. The ring alignment was characterized by Herman's orientation factor (HOF) of carbon rings. The HOF value was calculated for each microstructure using information on the orientation of five-, six-, and seven-member carbon rings with respect to the CF axis. The orientation of each carbon ring is defined by a vector that is normal to the plane of a ring. In this approach, an HOF value of −0.5 indicates perfect alignment of the carbon rings along the fiber axis (*x*-axis in simulations), and the HOF value of 0.0 indicates random alignment of carbon rings.

3. RESULTS AND DISCUSSION

3.1. Morphology and Structure Characterization of CFs. In this study, stabilized PAN fibers were carbonized at three separate temperatures to investigate the effect of carbonization temperature on fiber morphology and structural developments. The diameter of the fiber shrank gradually with increasing carbonization temperature from a maximum average diameter of 8.0 μm at 1800 K to a minimum of 6.6 μm at 2800 K, which is because a larger number of small molecules is released at higher carbonization temperatures. Microscopic observations (Figure 3a−f and Figure S1), elemental analysis (as shown in Table S1), and XPS analysis (Figure S2) are also consistent with this result. The weight content of carbon (C) increased from 97.19% to 98.55% as the carbonization temperature rose from 1800 to 2800 K. Several randomly distributed graphitic layers with length of 4−5 nm can be identified in the HRTEM image (Figure 3d) of the CF carbonized at 1800 K. As the carbonization temperature went up to 2800 K (Figure 3f), the amount and size of ordered graphitic layers increased significantly, demonstrating the development of the graphitic structure and resulting in an

DOI: 10.1021/acsami.9b15833
ACS Appl. Mater. Interfaces 2019, 11, 42288−42297

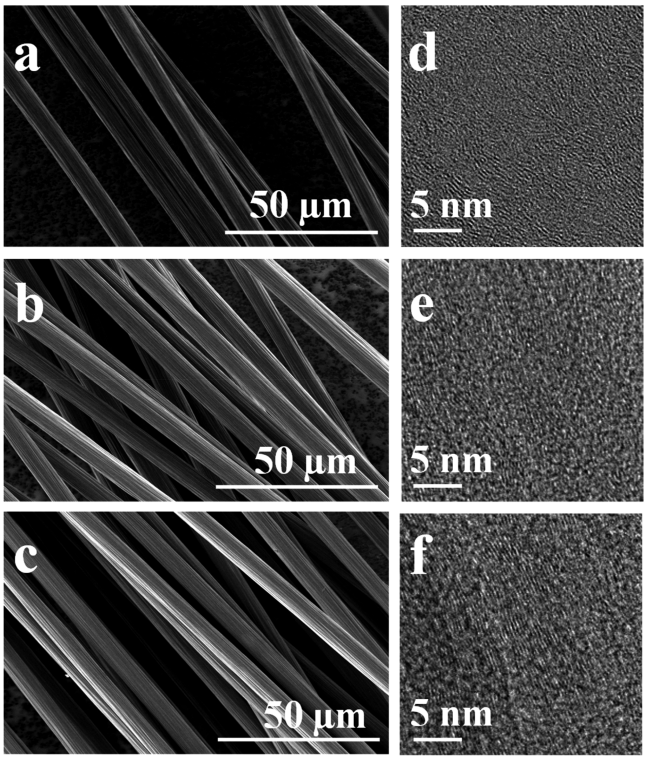

Figure 3. SEM and HR-TEM images of the CFs carbonized at (a,d) 1800 K; (b,e) 2300 K; and (c,f) 2800 K.

increase of the CFs' density, up to 1.858 g cm^{-3} for the CFs carbonized at 2800 K (summarized in Table S2).

The XRD patterns of CFs in Figure 4a present a weak and broad peak at 2θ of 24.25°, corresponding to the graphitic (002) plane, a characteristic of disordered carbon material.[64] The interlayer spacing (d_{002}) in CFs (Table S3, calculated by Bragg's law) indicates that with the increase in carbonization temperature from 1800 to 2800 K, the interlayer spacing decreases linearly from 0.350 to 0.340 nm due to the changes in the microstructure of the CFs. It should be noted that the peaks at 2θ of 43.4° and 53.7°, which are ascribed to the graphitic (101) and (004) planes, respectively, become obvious with the increment of carbonization temperatures due to the increasing size of the graphitic crystallites within the CF microstructure.

To study the degree of graphitization of the as-prepared CFs, Raman spectra were recorded as shown in Figure 4b. The broad D (defects or disordered regions) and G bands (ordered graphitic structure) indicate that all studied CFs contain partially graphitized carbon along with amorphous carbon.[65] The graphitized carbon regions are small and generally consist of several graphitic layers. The relative intensity ratio (I_D/I_G) between the D and G bands indicates the degree of the disorder within the carbon structure. Among the studied CFs, the I_D/I_G ratio decreases with increasing carbonization temperature in Table S3, representing the transformation of disordered carbon into graphitic carbon at higher temperatures. However, it is noteworthy that the coexistence of the prominent D band and a wide G band suggests a loss of long-range ordering between the graphene sheets. Meanwhile, it is obvious that the intensity of the 2D peak ascribed to the second-order Raman band becomes sharper with the increment of carbonization temperature, which is related to the growth of the graphite crystal structure.[66] This result is consistent with the results of the XRD and TEM analyses discussed above.

3.2. Atomistic Modeling of the Carbonization Process. To gain an atomistic perspective regarding the evolution of the graphitic structure during the initial stage of the carbonization process, we performed MD simulations of the oxidized PAN polymers (see Figure 1a) using the ReaxFF method. The details of the carbonization simulations are described in section 2.3.1. In Figure 1a, the snapshots for one of the samples, consisting of 16 oxidized PAN chains, are presented for each carbonization temperature. From these simulation snapshots, we can observe the formation of all-carbon, six-membered rings after 1 ns of the simulations at higher carbonization temperatures. The quantitative analysis of the production of the all-carbon, five/six/seven-membered rings is given in Figure 5. For the lowest temperature, 1800 K, we do not see significant ring production; this outcome essentially reflects the limitations of atomistic simulations and the necessity to simulate systems at higher temperatures to speed up the dynamics and observe reactions involved in the formation of the carbon rings at a pico- to nanoseconds scale. All-carbon ring production can be seen at 2300 and 2800 K. For both systems and for all considered carbon rings, the trend is the same: higher carbonization temperature results in higher rate of the ring production. Moreover, we clearly see that more six-membered rings are produced as compared to five- or seven-membered rings for any of these carbonization temperatures, with a significant increase in six-membered ring production at 2800 K.

These rings tend to create clusters, which can serve as nucleation sites for the emergence of the graphitic structure. The growth of these ring clusters is most dominant in the samples with the highest carbonization temperature, 2800 K,

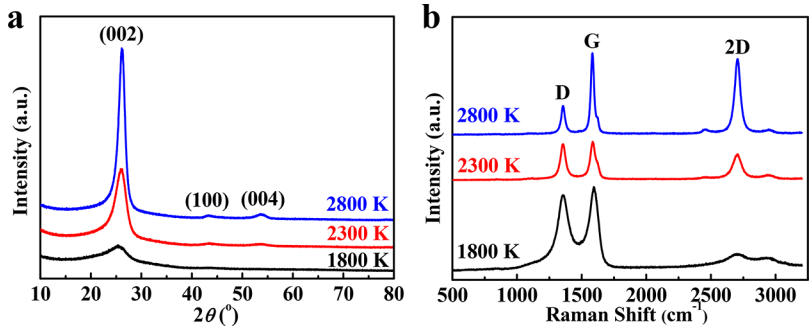

Figure 4. (a) XRD and (b) Raman patterns of the CFs carbonized at various temperatures.

DOI: 10.1021/acsami.9b15833
ACS Appl. Mater. Interfaces 2019, 11, 42288−42297

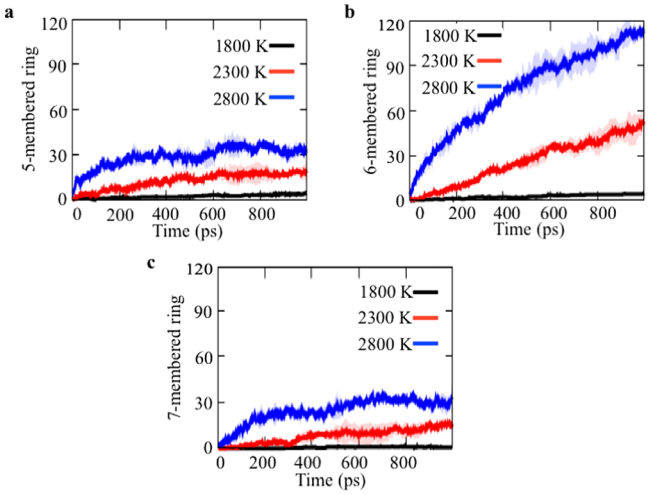

Figure 5. All-carbon rings production in ReaxFF MD simulations of carbonization of oxidized PAN polymers performed at three temperatures: 1800, 2300, and 2800 K. The production of the five-, six-, and seven-membered rings during the simulations is illustrated in (a), (b), and (c), respectively.

and this growth can be demonstrated by comparing the partial carbon−carbon radial distribution functions calculated for each sample after 1 ns of the simulation (Figure 6a). A significant increase in peak intensity is observed for the first three peaks with increased carbonization temperature. The first peak corresponds to the carbon−carbon bond distance, whereas the second peak can be related to the distance between carbon atoms that are the next nearest neighbors in a ring. The third peak at a distance of approximately 3.8 Å is associated with pairs of carbon atoms that belong to different carbon rings, as illustrated in the inset in Figure 6a. This peak is most pronounced for the sample generated at the highest temperature. Carbon atom pairs of this distance appear only after the clustering of carbon rings. These clusters of all-carbon rings are initially interconnected through a heteroatom network and show an increasing fraction of the carbon atoms during the cluster growth. Figure 5b shows the weight fraction of carbon atoms in the final cluster for each sample. Again, the simulation results are consistent with the experimental results discussed above: as the carbonization temperature is increased the percentage of carbon atoms increases as well, which may increase the formation of graphitic structure due to a greater release of other atoms. However, the fraction of the carbon atoms present in the final clusters obtained in any of the simulations does not exceed 75 wt %, which indicates an early stage of the carbonization process. Also, the released mass, which is the mass fraction of all small molecules produced during the simulations, increases with the carbonization temperature as can be seen from Figure 6b. Once again, a relatively small percentage of the released mass, less than 30 wt %, indicates that the simulations show only the early stage of the carbonization process. The released mass is composed of small molecules, such as hydrogen, nitrogen, water, carbon monoxide, carbon dioxide, ammonia, and hydrogen cyanide molecules, which are characteristic products from the stabilized PAN carbonization process.[58] The proposed production pathways for N_2 and H_2 release have been discussed in our previous work.[53] Despite the fact that only the initial stage of the carbonization process is simulated, the increase in gas release with increase in carbonization temperature supports the experimental results showing that the fiber diameter decreased with increasing carbonization temperature.

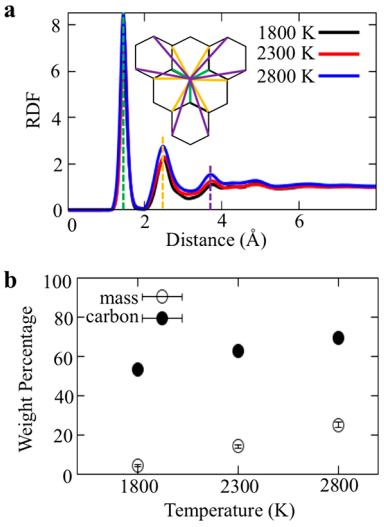

Figure 6. Analysis of the final stage of the simulated carbonization processes. (a) The comparison of the partial carbon−carbon radial distribution function (RDF) calculated after 1 ns of the simulations of the carbonization at temperatures of 1800, 2300, and 2800 K. A schematic all-carbon six-membered ring cluster is presented in the middle of the graph. The distances corresponding to the peaks in the RDF are indicated on this scheme using the same colors as the dashed lines: green for C−C bond distance; orange for the second nearest neighbor carbon atoms in the ring; and purple for the nearest distance between carbon atoms that belong to two adjacent carbon rings. (b) The weight fractions of carbon atoms present in the final cluster of carbon rings that appears during the carbonization process and the released mass in the form of small molecules.

3.3. Mechanical Properties of Carbonized PAN CFs.

Tensile properties of the processed CFs were measured using a single filament tester. The corresponding results are summarized in Table 1, and the typical stress−strain curves are shown in Figure S3. An average strength of 3.44 GPa and a strain at failure of 1.53% could be achieved at a carbonization temperature of 1800 K. The strength slightly decreases to 3.11 and 3.00 GPa, and the strain at failure decreases to 1.15% and 1.05% as the carbonization temperature rises to 2300 and 2800 K, respectively. Interestingly, Young's modulus increases from 269 to 298 GPa with increased carbonization temperatures (from 1800 to 2300 K) and further improves to 362 GPa at 2800 K.

Table 1. Tensile Properties of the Experimental CFs

carbonization temp (K)	strength (GPa)	Young's modulus (GPa)	strain (%)
1800	3.44 ± 0.30	269 ± 25	1.53 ± 0.27
2300	3.11 ± 0.26	298 ± 34	1.15 ± 0.13
2800	3.00 ± 0.21	362 ± 18	1.05 ± 0.06

To further understand the relationship between the mechanical properties and the microstructure, large-scale atomistic modeling of mechanical deformation was performed for the three computational samples shown in Figure 2. Before discussing the mechanical behavior, we first consider structural distinctions of the three samples as evidenced by the calculated

DOI: 10.1021/acsami.9b15833
ACS Appl. Mater. Interfaces 2019, 11, 42288−42297

XRD profiles shown in Figure 7 and structural parameters listed in Table 2.

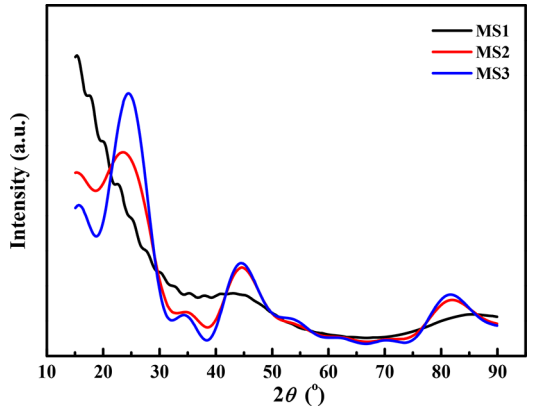

Figure 7. XRD profiles of simulated microstructures.

As can be seen from Figure 7, the XRD profile for the MS1 microstructure does not exhibit any discernible d_{002} peak, suggesting a very low degree of graphitization. This assertion is supported by direct calculation of the degree of graphitization, defined as the fraction of carbon atoms that belong to low-energy graphitic phase within the CF microstructure and listed in Table 2. The degree of graphitization is only 7.8%, and the microstructure contains only very small pockets of carbon atoms with graphite-like local environment. This computational sample also has the lowest density, which indicates a higher concentration of nanopores. These observed microstructural characteristics of sample MS1 are qualitatively similar to those discussed in section 3.1 for the experimental sample obtained at a low carbonization temperature of 1800 K.

The XRD profiles calculated for the other two microstructures, MS2 and MS3, show a noticeable d_{002} peak near $2\theta = 25°$, indicating the presence of sizable graphitic regions. Indeed, the values of the degree of graphitization listed in Table 2 for MS2 and MS3 are substantially higher than that of MS1, and nanoscale graphitic crystallites can be identified in the microstructure of these computational samples. The structural parameters of samples MS2 and MS3 are comparable to those of the experimental samples produced at higher carbonization temperatures of 2300 and 2800 K discussed in section 3.1: the higher is the carbonization temperature, the lower is the interlayer spacing.

The mechanical properties of the three computational microstructures are evaluated in tensile testing simulations performed by stretching the samples along the fiber axis (x-direction) at a strain rate of 2.5×10^8 s^{-1}. A constant pressure of 1 atm was maintained in the lateral (y and z) directions. The stress–strain curves and the corresponding mechanical properties of different microstructures are shown in Figure 8 and

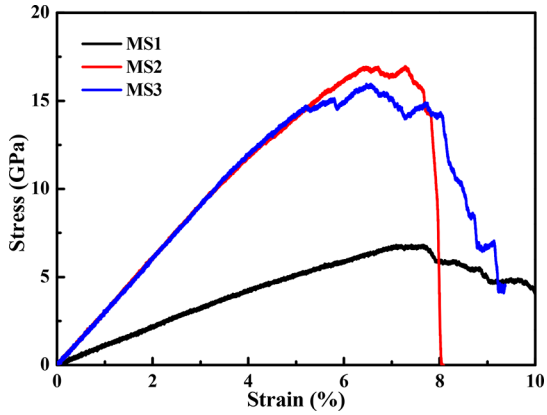

Figure 8. Stress–strain curves predicted in axial deformation of simulated microstructures.

listed in Table 3. It should be noted that MS1, MS2, and MS3 microstructures, which are used in estimating mechanical properties, contain only carbon atoms and hence have a carbon content of 100%.

Table 3. Tensile Properties of the Simulated Microstructures

microstructure	strength (GPa)	Young's modulus (GPa)	strain (%)
MS1	6.73	95.5	7.6
MS2	16.9	279.4	7.3
MS3	15.9	284.5	6.6

The MS1 microstructure, which does not contain any sizable regions of graphitic phase, exhibits a much softer response to tensile loading and has significantly lower Young's modulus as compared to other microstructures. The highest Young's modulus is observed for the MS3 microstructure, which contains the largest graphitic regions and features the highest overall graphite content. The results of tensile testing simulations show that Young's modulus is directly correlated with the degree of graphitization as well as the alignment of carbon rings as reflected by HOF listed in Table 2, while the failure strain is inversely correlated with those factors. These trends agree well with the experimental results discussed above. The absolute values of the tensile strength and failure strain of the simulated microstructures are considerably higher than the experimental values. These discrepancies are mainly due to the ultrahigh loading rate used in simulations and the length-scale differences. The simulated microstructures are at least 2 orders of magnitude smaller than the experimental samples, which imposes a much lower limit on the maximum pore size as compared to experimental samples. Larger pores in the experimental samples can serve as stress concentration sites that lead to brittle fracture at much lower levels of stress and strain.

Table 2. Density, d-Spacing, Graphite Crystallite Size, Degree of Graphitization, and Fiber Orientation in Different Microstructures Produced in Large-Scale Atomistic Simulations

					HOF	
microstructure	density (g cm^{-3})	d_{002} (nm)	crystallite size (nm)	degree of graphitization (%)	initial	final
MS1	1.63			7.8	−0.03	−0.11
MS2	1.80	3.78	1.49	18.5	−0.46	−0.39
MS3	1.93	3.62	2.11	31.2	−0.49	−0.39

DOI: 10.1021/acsami.9b15833
ACS Appl. Mater. Interfaces 2019, 11, 42288–42297

4. CONCLUSIONS

In this study, experimental characterization was coupled with multiscale modeling to provide insights into the influence of carbonization temperature on the structural and mechanical properties of the PAN-derived CFs. Atomistic scale ReaxFF simulations of the initial stage of carbonization of oxidized PAN samples were performed at various temperatures, and the temperature dependence of the production of all-carbon ring structures was analyzed. The sensitivity of the mechanical properties on CF microstructures was further investigated through large-scale MD simulations performed with a less computationally demanding AIREBO potential. The main conclusions obtained from the joint computational and experimental study are summarized as follows:

(1) Carbon content rises and fiber diameter decreases with increasing carbonization temperature, which is due to additional release of small molecules at higher temperatures and the development of carbon crystal structures. These results agree well with predictions of small-scale ReaxFF reactive MD simulations. For the same simulation time, higher carbonization temperature results in the formation of larger clusters of all-carbon rings. These all-carbon ring clusters are likely to serve as seeds for the growth of larger crystalline graphitic regions, suggesting that a higher degree of graphitization can be achieved for samples processed at higher temperatures.

(2) Large-scale MD simulations, performed to evaluate the effect of the CF microstructure on the mechanical properties, indicate that Young's modulus is directly correlated with the degree of graphitization and ring alignment. However, failure strain is inversely correlated with those factors. These observed trends agree well with experimental observations.

Overall, the carbonization temperature was found to play a key role in the development of graphitic regions within the CF microstructure, which significantly influences the final mechanical properties of the prepared CFs. By combining experimental characterization with computer simulations, a valuable computational framework has been established to not only provide guidance for the optimization of large-scale production lines but also to assist in the search for alternative low-cost CF precursors, which in turn facilitates the practical applications of CFs in EVs and AVs to meet the rapidly increasing demand from customers.

■ ASSOCIATED CONTENT

Supporting Information

The Supporting Information is available free of charge on the ACS Publications website at DOI: 10.1021/acsami.9b15833.

Cross-sectional SEM images of individual CFs carbonized at different temperatures; XPS profiles of the obtained CFs; typical stress−strain curves of the experimental CFs; elemental analysis of the prepared CFs; densities of the oxidized PAN and carbonized fibers; and physical parameters of the prepared CFs (PDF)

■ AUTHOR INFORMATION

Corresponding Authors

*E-mail: lz2n@virginia.edu.
*E-mail: acv13@psu.edu.
*E-mail: xl3p@virginia.edu.

ORCID

Jiadeng Zhu: 0000-0003-4709-4115
Zan Gao: 0000-0003-3047-5616
Chowdhury M. Ashraf: 0000-0002-7375-2540
Leonid V. Zhigilei: 0000-0002-1549-7086
Adri C. T. van Duin: 0000-0002-3478-4945

Notes

The authors declare no competing financial interest.

■ ACKNOWLEDGMENTS

We gratefully acknowledge support from the U.S. Department of Energy (DOE), Vehicle Technologies Office, under contract number DE-EE0008195.

■ REFERENCES

(1) Endo, M.; Kim, Y. A.; Hayashi, T.; Nishimura, K.; Matusita, T.; Miyashita, K.; Dresselhaus, M. S. Vapor-Grown Carbon Fibers (VGCFs): Basic Properties and Their Battery Applications. *Carbon* **2011**, *39*, 1287−1297.

(2) Kadla, J. F.; Kubo, S.; Venditti, R. A.; Gilbert, R. D.; Compere, A. L.; Griffith, W. Lignin-Based Carbon Fibers for Composite Fiber Applications. *Carbon* **2002**, *40*, 2913−2920.

(3) Zhu, J.; Chen, C.; Lu, Y.; Zang, J.; Jiang, M.; Kim, D.; Zhang, X. Highly Porous Polyacrylonitrile/Graphene Oxide Membrane Separator Exhibiting Excellent Anti-Self-Discharge Feature for High-Performance Lithium-Sulfur Batteries. *Carbon* **2016**, *101*, 272−280.

(4) Islam, M. S.; Deng, Y.; Tong, L.; Faisal, S. N.; Roy, A. K.; Minett, A. I.; Gomes, V. G. Grafting Carbon Nanotubes directly onto Carbon Fibers for Superior Mechanical Stability: Towards Next Generation Aerospace Composites and Energy Storage Applications. *Carbon* **2016**, *96*, 701−710.

(5) Xu, Z.; Gao, C. Graphene Fiber: A New Trend in Carbon Fibers. *Mater. Today* **2015**, *18*, 480−492.

(6) Li, Y.; Zhu, J.; Zhu, P.; Yan, C.; Jia, H.; Kiyak, Y.; Zang, J.; He, J.; Dirican, M.; Zhang, X. Ultrafine and Polar ZrO_2-Inlaid Porous Nitrogen-Doped Carbon Nanofiber as Efficient Polysulfide Absorbent for High-Performance Lithium-Sulfur Batteries with Long Lifespan. *Chem. Eng. J.* **2018**, *349*, 376−387.

(7) Chen, C.; Li, G.; Zhu, J.; Lu, Y.; Jiang, M.; Hu, Y.; Shen, Z.; Zhu, P.; Zhang, X. In-Situ Formation of Tin-Antimony Sulfide in Nitrogen-Sulfur Co-Doped Carbon Nanofibers as High Performance Anode Materials for Sodium-Ion Batteries. *Carbon* **2017**, *120*, 380−391.

(8) Li, Y.; Zhu, J.; Zhu, P.; Yan, C.; Jia, H.; Kiyak, Y.; Zang, J.; He, J.; Dirican, M.; Zhang, X. Glass Fiber Separator Coated by Porous Carbon Nanofiber Derived from Immiscible PAN/PMMA for High-Performance Lithium-Sulfur Batteries. *J. Membr. Sci.* **2018**, *552*, 31−42.

(9) Wang, Y.; Xu, L.; Wang, M.; Pang, W.; Ge, X. Structural Identification of Polyacrylonitrile during Thermal Treatment by Selective ^{13}C Labeling and Solid-State ^{13}C NMR Spectroscopy. *Macromolecules* **2014**, *47*, 3901−3908.

(10) Frank, E.; Steudle, L. M.; Ingildeev, D.; Spoerl, J. M.; Buchmeiser, M. R. Carbon Fibers: Precursor Systems, Processing, Structure, and Properties. *Angew. Chem., Int. Ed.* **2014**, *53*, 5262−5298.

(11) Frank, E.; Hermanutz, F.; Buchmeiser, M. R. Carbon Fibers: Precursors, Manufacturing, and Properties. *Macromol. Mater. Eng.* **2012**, *297*, 493−501.

(12) Bhat, G. *Structure and Properties of High-Performance Fibers*; Woodhead Publishing: UK, 2016.

(13) Frank, E.; Buchmeiser, M. R. Carbon Fibers. *Encyclopedia of Polymeric Nanomaterials*; Springer: New York, 2015; pp 306−310.

(14) Buchmeiser, M. R.; Muks, E.; Schowner, R.; Frank, E.; Hageroth, U.; Henzler, S.; Spörl, J.; Ota, A.; Beyer, R.; Müller, A. Structure Evolution in All-Aromatic, Poly (p-phenylene-vinylene)-Derived Carbon Fibers. *Carbon* **2019**, *144*, 659−665.

DOI: 10.1021/acsami.9b15833
ACS Appl. Mater. Interfaces 2019, 11, 42288−42297

(15) Ma, L.; Zhu, Y.; Wang, M.; Yang, X.; Song, G.; Huang, Y. Enhancing Interfacial Strength of Epoxy Resin Composites via Evolving Hyperbranched Amino-Terminated POSS on Carbon Fiber Surface. *Compos. Sci. Technol.* **2019**, *170*, 148−156.
(16) Ma, L.; Li, N.; Wu, G.; Song, G.; Li, X.; Han, P.; Wang, G.; Huang, Y. Interfacial Enhancement of Carbon Fiber Composites by Growing TiO_2 Nanowires onto Amine-Based Functionalized Carbon Fiber Surface in Supercritical Water. *Appl. Surf. Sci.* **2018**, *433*, 560−567.
(17) Ma, L.; Zhu, Y.; Feng, P.; Song, G.; Huang, Y.; Liu, H.; Zhang, J.; Fan, J.; Hou, H.; Guo, Z. Reinforcing Carbon Fiber Epoxy Composites with Triazine Derivatives Functionalized Graphene Oxide Modified Sizing Agent. *Composites, Part B* **2019**, *176*, 107078-1−10.
(18) Li, Y.; Zhang, T.; Jiang, B.; Zhao, L.; Liu, H.; Zhang, J.; Fan, J.; Guo, Z.; Huang, Y. Interfacially Reinforced Carbon Fiber Silicone Resin via Constructing Functional Nano-Structural Silver. *Compos. Sci. Technol.* **2019**, *181*, 107689-1−6.
(19) Wu, Z.; Cui, H.; Chen, L.; Jiang, D.; Weng, L.; Ma, Y.; Li, X.; Zhang, X.; Liu, H.; Wang, N.; Zhang, J.; Ma, Y.; Zhang, M.; Huang, Y.; Guo, Z. Interfacially Reinforced Unsaturated Polyester Carbon Fiber Composites with a Vinyl Ester-Carbon Nanotubes Sizing Agent. *Compos. Sci. Technol.* **2018**, *164*, 195−203.
(20) Song, B.; Wang, T.; Wang, L.; Liu, H.; Mai, X.; Wang, X.; Wang, N.; Huang, Y.; Ma, Y.; Lu, Y.; Wujcik, E. K.; Guo, Z. Interfacially Reinforced Carbon Fiber/Epoxy Composite Laminates via In-Situ Synthesized Graphitic Carbon Nitride (g-C_3N_4). *Composites, Part B* **2019**, *158*, 259−268.
(21) Zhu, J.; Park, S. W.; Joh, H. I.; Kim, H. C.; Lee, S. Preparation and Characterization of Isotropic Pitch-Based Carbon Fiber. *Carbon Lett.* **2013**, *14*, 94−98.
(22) Zhu, J.; Park, S. W.; Joh, H. I.; Kim, H. C.; Lee, S. Study on the Stabilization of Isotropic Pitch Based Fibers. *Macromol. Res.* **2015**, *23*, 79−85.
(23) Lee, S.; Kim, J.; Ku, B. C.; Kim, J.; Joh, H. I. Structural Evolution of Polyacrylonitrile Fibers in Stabilization and Carbonization. *Adv. Chem. Eng. Sci.* **2012**, *2*, 275−282.
(24) Lee, S. H.; Kim, J. H.; Ku, B. C.; Kim, J. K.; Chung, Y. S. Effect of Process Condition on Tensile Properties of Carbon Fiber. *Carbon Lett.* **2011**, *12*, 26−30.
(25) Song, B.; Wang, T.; Sun, H.; Liu, H.; Mai, X.; Wang, X.; Wang, L.; Wang, N.; Huang, Y.; Guo, Z. Graphitic Carbon Nitride (g-C_3N_4) Interfacially Strengthened Carbon Fiber Epoxy Composites. *Compos. Sci. Technol.* **2018**, *167*, 515−521.
(26) He, Y.; Chen, Q.; Yang, S.; Lu, C.; Feng, M.; Jiang, Y.; Cao, G.; Zhang, J.; Liu, C. Micro-Crack Behavior of Carbon Fiber Reinforced Fe_3O_4/Graphene Oxide Modified Epoxy Composites for Cryogenic Application. *Composites, Part A* **2018**, *108*, 12−22.
(27) Li, D.; Lu, C.; Wang, L.; Du, S.; Yang, Y. A Reconsideration of the Relationship between Structural Features and Mechanical Properties of Carbon Fibers. *Mater. Sci. Eng., A* **2017**, *685*, 65−70.
(28) Kim, M. A.; Jang, D.; Tejima, S.; Cruz-Silva, R.; Joh, H. I.; Kim, H. C.; Lee, S.; Endo, M. Strengthened PAN-Based Carbon Fibers Obtained by Slow Heating Rate Carbonization. *Sci. Rep.* **2016**, *6*, 22988-1−7.
(29) Mortensen, A., Ed. *Concise Encyclopedia of Composite Materials*; Elsevier: New York, 2006.
(30) Chawla, K. K. *Composite Materials: Science and Engineering*; Springer Science & Business Media: New York, 2012.
(31) Newcomb, B. A. Processing, Structure, and Properties of Carbon Fibers. *Composites, Part A* **2016**, *91*, 262−282.
(32) Zhao, J.; Wu, L.; Zhan, C.; Shao, Q.; Guo, Z.; Zhang, L. Overview of Polymer Nanocomposites: Computer Simulation Understanding of Physical Properties. *Polymer* **2017**, *133*, 272−287.
(33) Rahaman, M. S. A.; Ismail, A. F.; Mustafa, A. A Review of Heat Treatment on Polyacrylonitrile Fiber. *Polym. Degrad. Stab.* **2007**, *92*, 1421−1432.
(34) Saha, B.; Schatz, G. C. Carbonization in Polyacrylonitrile (PAN) Based Carbon Fibers Studied by ReaxFF Molecular Dynamics Simulations. *J. Phys. Chem. B* **2012**, *116*, 4684−4692.
(35) Zhang, W.; Liu, J.; Gang, W. Evolution of Structure and Properties of PAN Precursors during Their Conversion to Carbon Fibers. *Carbon* **2003**, *41*, 2805−2812.
(36) Zussman, E.; Chen, X.; Ding, W.; Calabri, L.; Dikin, D. A.; Quintana, J. P.; Ruoff, R. S. Mechanical and Structural Characterization of Electrospun PAN-Derived Carbon Nanofibers. *Carbon* **2005**, *43*, 2175−2185.
(37) Kim, S. Y.; Lee, S.; Park, S.; Jo, S. M.; Lee, H. S.; Joh, H. I. Continuous and Rapid Stabilization of Polyacrylonitrile Fiber Bundles Assisted by Atmospheric Pressure Plasma for Fabricating Large-Tow Carbon Fibers. *Carbon* **2015**, *94*, 412−416.
(38) Kim, S. Y.; Kim, S. Y.; Lee, S.; Jo, S.; Im, Y. H.; Lee, H. S. Microwave Plasma Carbonization for the Fabrication of Polyacrylonitrile-Based Carbon Fiber. *Polymer* **2015**, *56*, 590−595.
(39) Zhu, J.; Yan, C.; Zhang, X.; Yang, C.; Jiang, M.; Zhang, X. A Sustainable Platform of Lignin: From Bioresources to Materials and Their Applications in Rechargeable Batteries and Supercapacitors. *Prog. Energy Combust. Sci.* **2020**, *76*, 100788-1−24.
(40) Chen, J. C.; Harrison, I. R. Modification of Polyacrylonitrile (PAN) Carbon Fiber Precursor via Post-Spinning Plasticization and Stretching in Dimethyl Formamide (DMF). *Carbon* **2002**, *40*, 25−45.
(41) Edie, D. D. The Effect of Processing on the Structure and Properties of Carbon Fibers. *Carbon* **1998**, *36*, 345−362.
(42) Fitzer, E. Pan-Based Carbon Fibers-Present State and Trend of the Technology from the Viewpoint of Possibilities and Limits to Influence and to Control the Fiber Properties by the Process Parameters. *Carbon* **1989**, *27*, 621−645.
(43) Wang, S.; Chen, Z. H.; Ma, W. J.; Ma, Q. S. Influence of Heat Treatment on Physical-Chemical Properties of PAN-Based Carbon Fiber. *Ceram. Int.* **2006**, *32*, 291−295.
(44) Naito, K. Y. T.; Yang, J. M.; Kagawa, Y. Tensile Properties of Ultrahigh Strength PAN-Based, Ultrahigh Modulus Pitch-Based and High Ductility Pitch-Based Carbon Fibers. *Carbon* **2008**, *46*, 189−195.
(45) Kamat, A. M.; van Duin, A. C. T.; Yakovlev, A. Molecular Dynamics Simulations of Laser-Induced Incandescence of Soot Using an Extended ReaxFF Reactive Force Field. *J. Phys. Chem. A* **2010**, *114*, 12561−12572.
(46) Saha, B.; Dzenis, Y.; Schatz, G. C. Multi-Step Mechanism of Carbonization in Templated Polyacrylonitrile Derived Fibers: ReaxFF Model Uncovers Origins of Graphite Alignment. *Carbon* **2015**, *94*, 694−704.
(47) Gupta, A.; Harrison, I. R. New Aspects in the Oxidative Stabilization of PAN-Based Carbon Fibers. *Carbon* **1996**, *34*, 1427−1445.
(48) Lee, S. W.; Lee, H. Y.; Jang, S. Y.; Jo, S.; Lee, H. S.; Choe, W. H.; Lee, S. Efficient Preparation of Carbon Fibers Using Plasma Assisted Stabilization. *Carbon* **2013**, *55*, 361−365.
(49) Desai, S.; Li, C.; Shen, T.; Strachan, A. Molecular Modeling of the Microstructure Evolution during Carbon Fiber Processing. *J. Chem. Phys.* **2017**, *147*, 224705-1−10.
(50) Brenner, D. W.; Shenderova, O. A.; Harrison, J. A.; Stuart, S. J.; Ni, B.; Sinnott, S. B. A. A Second-Generation Reactive Empirical Bond Order (REBO) Potential Energy Expression for Hydrocarbons. *J. Phys.: Condens. Matter* **2002**, *14*, 783−802.
(51) Tersoff, J. Empirical Interatomic Potential for Carbon, with Applications to Amorphous Carbon. *Phys. Rev. Lett.* **1988**, *61*, 2879−2882.
(52) Senftle, T. P.; Hong, S.; Islam, M. M.; Kylasa, S. B.; Zheng, Y.; Shin, Y. K. The ReaxFF Reactive Force-Field: Development, Applications and Future Directions. *NPJ. Comput. Mater.* **2016**, *2*, 15011-1−14.
(53) Kowalik, M.; Ashraf, C.; Damirchi, B.; Akbarian, D.; Rajabpour, S.; van Duin, A. C. T. Atomistic Scale Analysis of the Carbonization Process for C/H/O/N-Based Polymers with the ReaxFF Reactive Force Field. *J. Phys. Chem. B* **2019**, *123*, 5357−5367.

DOI: 10.1021/acsami.9b15833
ACS Appl. Mater. Interfaces 2019, 11, 42288−42297

(54) Morita, K.; Murata, Y.; Ishitani, A.; Murayama, K.; Ono, T.; Nakajima, A. Characterization of Commercially Available PAN (polyacrylonitri1e)-Based Carbon Fibers. *Pure Appl. Chem.* **1986**, *58*, 455−468.
(55) Srinivasan, S. G.; van Duin, A. C. T.; Ganesh, P. Development of a ReaxFF Potential for Carbon Condensed Phases and Its Application to the Thermal Fragmentation of a Large Fullerene. *J. Phys. Chem. A* **2015**, *119*, 571−580.
(56) Ashraf, C.; van Duin, A. C. T. Extension of the ReaxFF Combustion Force Field toward Syngas Combustion and Initial Oxidation Kinetics. *J. Phys. Chem. A* **2017**, *121*, 1051−1068.
(57) *ADF Modeling Suite, SCM*; Theoretical Chemistry, Vrije Universiteit: Amsterdam, The Netherlands, 2017.
(58) Morgan, P. *Carbon Fibers and Their Composites*; CRC Press: New York, 2005.
(59) Humphrey, W.; Dalke, A.; Schulten, K. VMD: Visual Molecular Dynamics. *J. Mol. Graphics* **1996**, *14*, 33−38.
(60) Joshi, K.; Arefev, M. I.; Zhigilei, L. V. Generation and Characterization of Carbon Fiber Microstructure in Atomistic Simulations. *Carbon* **2019**, *152*, 396−408.
(61) Martínez, L.; Andrade, R.; Birgin, E. G.; Martínez, J. M. PACKMOL: A Package for Building Initial Configurations for Molecular Dynamics Simulations. *J. Comput. Chem.* **2009**, *30*, 2157−2164.
(62) O'Connor, T. C.; Andzelm, J.; Robbins, M. O. AIREBO-M: A Reactive Model for Hydrocarbons at Extreme Pressures. *J. Chem. Phys.* **2015**, *142*, 024903-1−9.
(63) Plimpton, S. Fast Parallel Algorithms for Short-Range Molecular Dynamics. *J. Comput. Phys.* **1995**, *117*, 1−19.
(64) Zhu, J.; Lu, Y.; Chen, C.; Ge, Y.; Jasper, S.; Leary, J. D.; Li, D.; Jiang, M.; Zhang, X. Porous One-Dimensional Carbon/Iron Oxide Composite for Rechargeable Lithium-Ion Batteries with High and Stable Capacity. *J. Alloys Compd.* **2016**, *672*, 79−85.
(65) Zhu, J.; Chen, C.; Lu, Y.; Ge, Y.; Jiang, H.; Fu, K.; Zhang, X. Nitrogen-Doped Carbon Nanofibers Derived from Polyacrylonitrile for Use as Anode Material in Sodium-Ion Batteries. *Carbon* **2015**, *94*, 189−195.
(66) Jiao, L.; Zhang, L.; Wang, X.; Diankov, G.; Dai, H. Narrow Graphene Nanoribbons from Carbon Nanotubes. *Nature* **2009**, *458*, 877−880.

DOI: 10.1021/acsami.9b15833
ACS Appl. Mater. Interfaces 2019, 11, 42288−42297